NANO LETTERS

Letter

pubs.acs.org/NanoLett

Deviatoric Stress-Driven Fusion of Nanoparticle Superlattices

Wenbin Li,[†] Hongyou Fan,[‡] and Ju Li*[,§,†]

[†]Department of Materials Science and Engineering, Massachusetts Institute of Technology, Cambridge, Massachusetts 02139, United States

[‡]Advanced Materials Laboratory, Sandia National Laboratories, 1001 University Boulevard SE, Albuquerque, New Mexico 87106, United States

[§]Department of Nuclear Science and Engineering, Massachusetts Institute of Technology, Cambridge, Massachusetts 02139, United States

Supporting Information

ABSTRACT: We model the mechanical response of alkanethiol-passivated gold nanoparticle superlattice (supercrystal) at ambient and elevated pressures using large-scale molecular dynamics simulation. Because of the important roles of soft organic ligands in mechanical response, the supercrystals exhibit entropic viscoelasticity during compression at ambient pressure. Applying a hydrostatic pressure of several hundred megapascals on the superlattice, combined with a critical deviatoric stress of the same order along the [110] direction of the face-centered-cubic supercrystal, can drive the room-temperature sintering ("fusion") of gold nanoparticles into ordered gold nanowire arrays. We discuss the molecular-level mechanism of such phenomena and map out a nonequilibrium stress-driven processing diagram, which reveals a region in stress space where fusion of nanoparticles can occur, instead of other competing plasticity or phase transformation processes in the supercrystal. We further demonstrate that, for silver−gold (Ag−Au) binary nanoparticle superlattices in sodium chloride-type superstructure, stress-driven fusion along the [100] direction leads to the ordered formation of Ag−Au multijunction nanowire arrays.

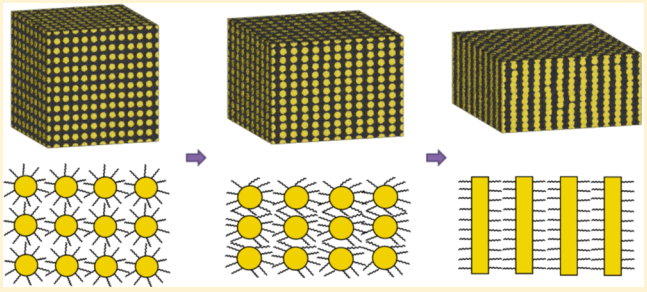

KEYWORDS: *Entropic viscoelasticity, ligand diffusion, room-temperature sintering, nanowire array, processing diagram*

Colloidal nanocrystals of metals and semiconductors are usually passivated with organic ligands to prevent aggregation in solution. Monodisperse ligand-passivated nanocrystals can self-assemble into long-range ordered superstructures, often called nanoparticle superlattice (NPSL), supercrystal, or supracrystal. NPSLs have been the subject of intense research in recent years.[1] These soft-sphere colloidal supercrystals have much richer interparticle interactions than their hard-sphere counterparts, evidenced by the variety of crystal structures that can be formed in binary NPSLs.[2] Study of collective phenomena in these "artificial solids" is a frontier of materials research. Mechanical properties of NPSLs are emergent properties in the sense that they derive from the collective interaction of the constituent nanoparticles. The study of mechanical behavior of NPSLs has only begun, and several pioneering experimental studies have appeared.[3−7] However, detailed, molecular-level understanding of the mechanical behavior of NPSLs is still very limited. An interesting possibility is room-temperature sintering ("fusion") of passivated nanoparticles ("artificial atoms") under stress, akin to the nuclear fusion of real atoms under ultrahigh temperature and pressure. Recent experimental studies demonstrated that mechanical deformations of gold and PbS nanoparticle assemblies in a pressurized environment lead to the formation of extended nanostructures, such as gold nanowire array,[8] 3D nanostructured gold architecture,[9] and PbS nanosheet.[10] Yet the conditions under which such stress-driven transformations happen in NPSLs, as well as the associated molecular-level mechanisms, are not well understood.

In this work we carried out large-scale molecular dynamics (MD) simulations to study the mechanical behavior of gold NPSLs under both ambient and elevated pressures. We find that, due to the dominant roles of organic ligands in mechanical response,[5,6,11] the NPSLs exhibit entropic viscoelasticity during compressive deformation at ambient pressure. At moderately elevated stresses, our simulation confirms Wu et al.'s experimental report[8] that gold NPSLs can be transformed into ordered gold nanowire arrays via deviatoric stress driven sintering ("fusion") of gold nanoparticles in the NPSLs. The following stress conditions are required to enable such fusion: (a) the presence of a background hydrostatic pressure P of the order several hundred megapascal (MPa); (b) the presence of a critical deviatoric stress (uniaxial) τ in addition to the aforementioned hydrostatic pressure (triaxial) background.

Received: March 31, 2014
Revised: June 16, 2014
Published: July 30, 2014

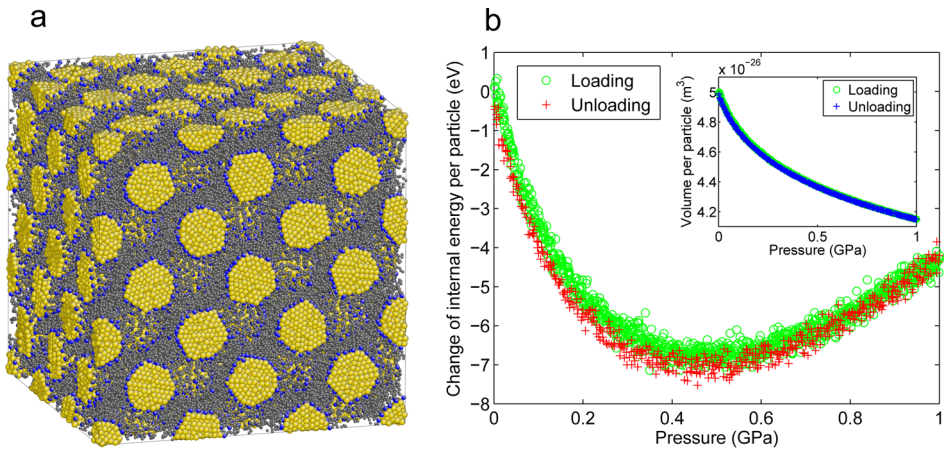

Figure 1. (a) Equilibrium configuration of octanethiol passivated gold NPSL at 300 K and zero pressure. The atoms depicted are gold (yellow), sulfur (blue), and carbon (gray). The system, which is primarily used for studies involving only hydrostatic pressure, contains 108 gold nanoparticles. (b) Internal energy change (ΔU) per nanoparticle during an isothermal compression−decompression cycle of gold NPSL at 300 K. Inset shows the change of volume per nanoparticle during the cycle.

The direction of the deviatoric stress should be properly aligned with the crystallographic direction of the superlattice. In face-centered cubic *fcc* structure, this is the [110] nearest-neighbor (Burgers vector) direction of nanoparticles in the superlattice. On the basis of these insights, we demonstrate that stress-driven fusion of silver−gold (Ag−Au) binary NPSLs can lead to the formation of Ag−Au multijunction nanowire arrays with similar kinds of stresses.

The structural units of the gold NPSLs in our simulation are alkanethiol-passivated gold nanocrystals. To achieve a balance between computational cost and experimental relevance, each icosahedron-shaped gold nanocrystal in our simulation has diameter $d \approx 3$ nm, containing 561 gold atoms and exhibiting only (111) surfaces. The nanocrystals are capped by octanethiols ($S(CH_2)_7CH_3$). The ligands are self-assembled and absorbed onto the gold nanocrystal surfaces via gold−sulfur interaction in MD simulation. The coverage density of ligand is 136 molecules per nanocrystal, which corresponds to full ligand coverage density for the gold nanocrystal under consideration.[12] Individual gold nanoparticles are subsequently arranged into NPSLs with *fcc* superstructure. Our extensive Parrinello−Rahman MD simulation[13,14] with variable size and shape of simulation box confirms that *fcc* is indeed the most stable superstructure for the system considered here. After equilibration, different mechanical loads are imposed on the superlattice. Periodic boundary conditions are employed. The size of the simulation system is chosen based on the mechanical behavior under investigation. When plastic deformation is involved, the system typically contains more than 2500 nanoparticles. Detailed simulation methodology and procedures can be found in the Supporting Information.

Figure 1a shows a typical molecular configuration of the gold NPSLs. We compute the full elastic tensor of the NPSL at 300 K using strain fluctuation method.[11,15,16] The computed three independent elastic constants are $C_{11} = 1.18$ GPa, $C_{12} = 1.15$ GPa, and $C_{44} = 68$ MPa at $P = 0$, and the bulk modulus $B = 1.16$ GPa. Compared to simple atomic elastic solids,[17] the ratio of C_{44}/B is smaller by an order of magnitude, which however is reminiscent of complex fluids. The computed elastic moduli are in close agreement with Landman and Luedtke's simulation of gold NPSLs,[11] although in their study, the gold nanocrystals are modeled as undeformable rigid bodies. The correspondence can be accounted by the much higher mechanical rigidity of metallic gold compared to the organic ligands, resulting in the dominance of ligands in the mechanical response of the NPSLs at ambient pressure.[5,6]

Indeed, we find the NPSLs exhibit polymer-like entropic viscoelasticity during compressive deformation at low pressure. Figure 1b shows the change of internal energy per nanoparticle of the NPSLs during an isothermal compression−decompression cycle at 300 K, for hydrostatic pressure P varied between zero to 1 GPa. The initial configuration is fully equilibrated at zero external stress in the constant temperature, constant stress, and particle number (TtN) ensemble[14,16,18,19] for 20 ns, before cycling pressure in the ensemble over a 10 ns simulation period. When the pressure is lower than 0.5 GPa, the internal energy U of the system decreases, while the pressure is increased. This behavior is contrary to that of enthalpy-dominated hard materials like simple metals. While mechanical work W is continuously done to the system, the system dumps *more* heat to the environment (thermostat), $\Delta Q = \Delta U - \Delta W < 0$. If the compression is performed quasi-statically (without dissipation) and reversibly, $T\Delta S = \Delta Q$, then the system entropy must decrease rapidly. Analysis of the loading−unloading cycle indicates that the heat exchange is mainly due to entropy reduction (dissipation is small), and $T|\Delta S| \gg |\Delta U|$, which is the defining characteristics of entropy-dominated (instead of enthalpy-dominated) elasticity. As shown in Figure 1b, after loading and unloading, the potential energy and volume of the system almost return to the initial values. The remaining differences of potential energy and enthalpy between the initial and final configurations can be eliminated after equilibrating the system at zero pressure for another 1 ns. The small hysteresis during the loading−unloading cycle indicates that most of the mechanical work performed on the system is not dissipated, and $|\Delta Q| \approx T|\Delta S| \gg |\Delta U|$. Such entropic mechanical response is also observed in uniaxial compression of the NPSLs, albeit for uniaxial compression, viscoelasticity[3,6] and energy dissipation become more pronounced. The entropy reduction of the NPSLs during compressive deformation comes from the decrease of the configurational entropy of the ligands, which results from the significant reduction of free volume accessible to the ligands under compression (inset of Figure 1b). The simultaneous

dx.doi.org/10.1021/nl5011977 | *Nano Lett.* 2014, 14, 4951−4958

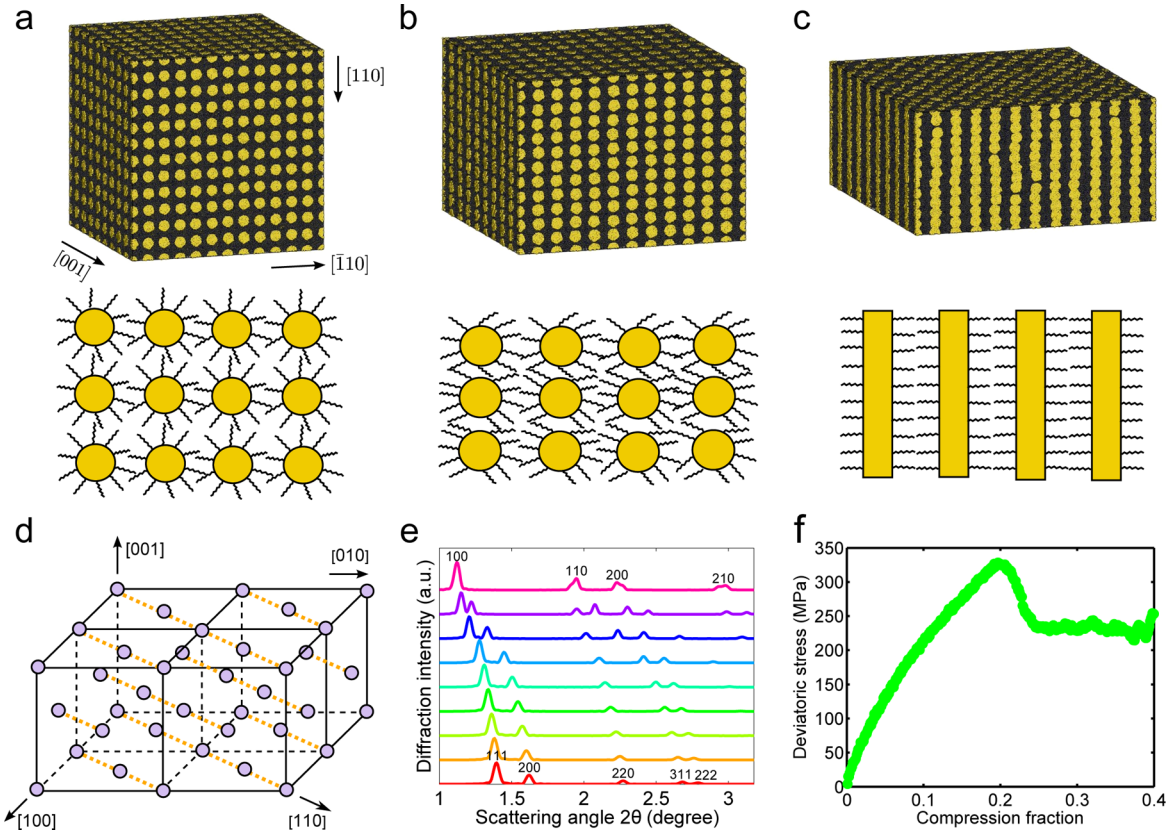

Figure 2. Stress-driven fusion of gold NPSL along the [110] direction of superlattice at 1 GPa pressure. (a–c) MD simulation snapshots and schematics showing the structural evolution of NPSL at different deformation stages. (a) Configuration of the system equilibrated at 1 GPa. The superlattice directions are labeled. (b) Configuration at engineering strain ε equal to −0.2. After deformation, neighboring nanoparticles become closer along the [110] direction. The process is accompanied by ligand conformation change and relocation. (c) Configuration at $\varepsilon = -0.4$. Most of the gold nanoparticles have fused together along the [110] direction and ordered nanowires are formed. (d) Lattice model of nanoparticle fusion along the [110] direction of *fcc* superlattice. Neighboring nanoparticles fuse along the dashed orange lines in the figure. (e) Evolution of SAXS patterns computed from simulation data. The incident beam passes along the [110] direction. Diffraction peaks due to the *fcc* superlattice (the bottom curve) and the nanowire array arranged in triangular lattice (the top curve) are labeled. The X-ray wavelength used for diffraction calculation is the same as in Wu et al.'s experiments.[8] (f) Deviatoric stress as a function of compression fraction (absolute value of strain).

decrease of potential energy comes from stronger van der Waals attraction between the ligands.[11] The total free energy change, given by $\Delta F = \Delta U - T\Delta S = \Delta Q + \Delta W - T\Delta S \approx \Delta W = -\int P\mathrm{d}V$, remains positive.

The structural stability of NPSLs under high pressure has been subjected to experimental studies recently.[9,20] However, whether purely hydrostatic pressure alone can induce fusion of NPSLs is still under debate. To help answer this question, we carry out hydrostatic deformation of gold NCSLs under high pressure. Starting with a fully equilibrated gold NPSL with the same configuration as in Figure 1a, we increase the normal stress components of the *T*t*N* ensemble (σ_{xx}, σ_{yy}, and σ_{zz}) from zero to 20 GPa over a simulation period of 20 ns, while setting the shear stress components of the ensemble (σ_{xy}, σ_{xz}, and σ_{yz}) to fluctuate around zero. This aims to simulate the hydrostatic compression of the NPSL in a fluid environment. The normal stresses of the ensemble are then kept at 20 GPa for another 5 ns. The simulation box is allowed to change in both size and shape. Over the entire course of the simulation, the system maintains *fcc* superstructure. No first-order phase transformation, nor fusion of nanoparticles, is observed. This is consistent with Podsiadlo et al.'s recent high pressure experiment, where they observed "nearly perfect structural stability" of PbS NPSL with *fcc* superlattice for pressure up to 12.5 GPa.[20] Our simulation also indicates that purely hydrostatic high pressures result in the jamming of ligands in gold NPSLs, reducing the ligands' surface diffusivity and preventing the gold nanoparticles from sintering with each other.

While high hydrostatic pressure alone does not induce the fusion of gold NPSLs in our simulation, we find that a moderate level of pressure, combined with a deviatoric stress τ of hundreds of MPa along an appropriate direction of the superlattice, transform the gold NPSLs into ordered gold nanowire arrays, which is consistent with previous experimental observation.[8] Uniaxial stresses along one of the three low-index directions of the *fcc* superlattice, namely, the [100], [111], and [110] directions, are considered. We build gold NPSLs with one of the low-index directions orienting along, for example, the *z* edge of the orthorhombic simulation box in Cartesian coordinates. The system, which includes around 2500 gold nanoparticles, is initially equilibrated in the *T*t*N* ensemble at zero stress. The pressure *P* of the system is then raised from zero to 1 GPa in the *T*t*N* ensemble over a period of 1 ns. This is followed by equilibration at 1 GPa for 2 ns, at the end of which large fluctuations in energy and volume have ceased. Subsequently, the *z* dimension of the simulation box is deformed with a fixed engineering strain rate of -1.0×10^{-4} per ps. Meanwhile, the σ_{xx} and σ_{yy} of the ensemble are controlled by barostat at 1 GPa, while σ_{xy}, σ_{xz}, and σ_{yz} are

dx.doi.org/10.1021/nl5011977 | *Nano Lett.* 2014, 14, 4951–4958

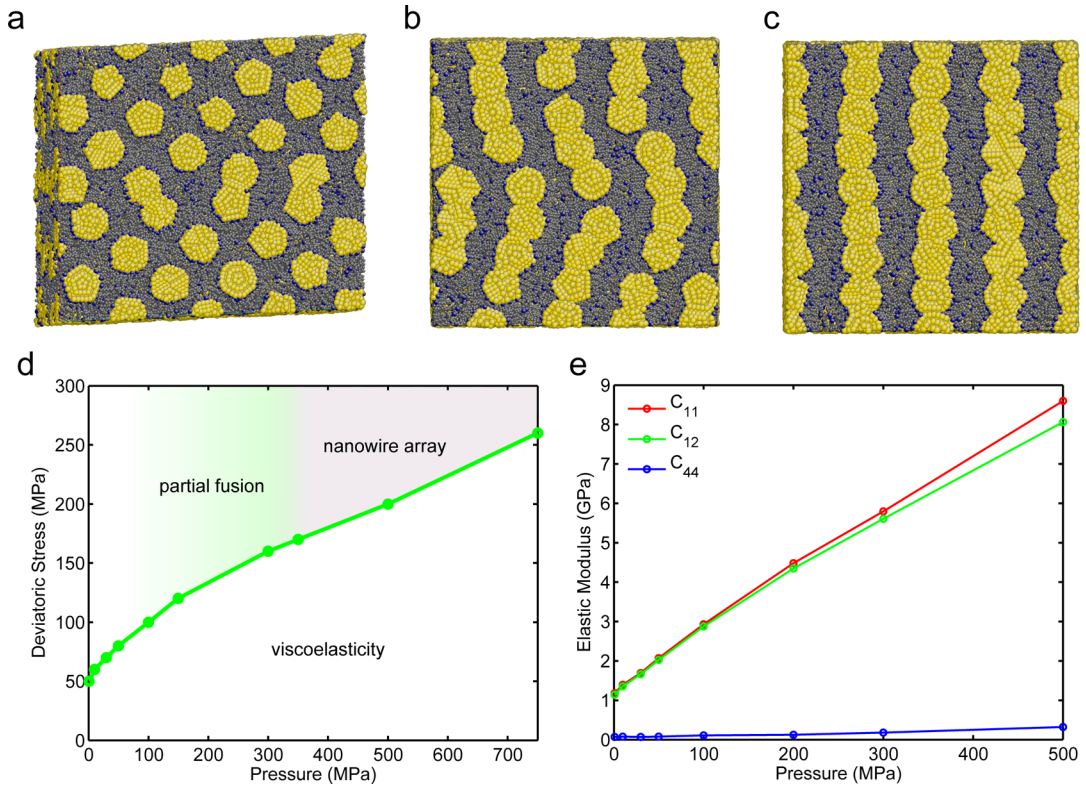

Figure 3. (a–c) Configurations of gold NPSLs at strain equal to −0.4 after uniaxial deformation along the [110] direction in the presence of different hydrostatic pressure. Panels a–c correspond to pressure equal to 100, 300, and 500 MPa, respectively. Gold nanoparticles are partially fused together along the [110] direction in panels a and b, while in panel c nanowire array is formed. (d) Nonequilibrium stress-driven fusion processing diagram of the simulated [110] oriented gold NPSL. The horizontal axis is the pressure applied on the system, while the vertical axis is the maximum deviatoric stress applied along the [110] direction during deformation. The green line represents the maximum deviatoric stress before fusion or mechanical yielding of NPSL at different pressure. By observing the configurations of the systems at the end of deformation, different regions in the stress space are determined and labeled in the diagram. Nanowire arrays are formed when both applied pressure and deviatoric stress exceed certain critical values. (e) Computed elastic moduli C_{11}, C_{12}, and C_{44} of the NPSL as a function of pressure.

controlled to be zero. This aims to simulate the uniaxial deformation of the NPSLs in the backdrop of a fluid-generated triaxial pressure. The deviatoric stress along the z direction is defined as $\tau \equiv \sigma_{zz} - P$. The engineering strain of deformation is calculated as $\varepsilon \equiv (L_z - L_{z0})/L_{z0}$, where L_{z0} and L_z are the lengths of the simulation box along the z direction at the beginning and during deformation, respectively.

For deformation along the [100] or [111] direction of the gold NPSLs, we could not observe ordered fusion of nanoparticles in the superlattices. Compressive stress along these two directions induces significant variation in the size and shape of the simulation box, indicating plasticity and/or phase transformation of the supercrystal, but the ordered fusion of nanoparticles does not occur (Supplementary Movies S1 and S2). We note that Wu et al. did not observe ordered fusion of [111] oriented gold NPSLs in their high pressure experiment[9] either.

For uniaxial compression along the [110] direction, however, we observe stress-driven fusion of gold nanoparticles into ordered gold nanowire array. The [110] direction is the nearest-neighbor direction of nanoparticles in *fcc* superlattice. Therefore, uniaxial compression along the [110] direction drives neighboring nanoparticles along this direction closer to each other. Uniaxial compression overcomes the entropic and steric repulsion of the ligands between the neighboring nanoparticles and eventually leads to the sintering of nanocrystal cores along the [110] direction. Ordered nanowire array forms as a result (Supplementary Movie S3). This process is illustrated in Figure 2. Figure 2a shows the configuration of the gold NPSLs before deformation. The schematic beneath illustrates the idealized configuration of the nanoparticles in the (001) plane of the superlattice. In Figure 2b, the engineering strain of the deformation reaches −0.2. The associated schematic shows the conformation change and reorganization of ligands on the nanocrystal surfaces, a picture supported by our detailed analysis (Supplementary Figure S1). When strain reaches −0.4 (Figure 2c), neighboring nanoparticles have overcome the passivation of ligands and attached to each other, forming ligand-passivated gold nanowire array.

In Figure 2d, we illustrate the fusion of NPSL in a crystallographic model. The fused nanoparticles form parallel nanowires along the [110] direction. Under compression, these wires pack closely into triangular lattice, with *P6mm* symmetry. The structural evolution is also captured by computing the small-angle X-ray scattering (SAXS) patterns during stress-driven fusion, which is shown in Figure 2e. The evolution of the SAXS patterns agrees with Wu et al.'s experimental data.[8] The critical deviatoric stress τ_{fusion} needed to drive fusion at P = 1 GPa pressure, as determined from the deviatoric stress versus engineering strain curve in Figure 2f, is around 330 MPa.

In addition to the orientation of superlattices, the existence of a moderate pressure background is found to be crucial for ordered fusion of NPSLs. We carry out uniaxial deformation of [100], [111], and [110] oriented superlattices at P = 0. In all

dx.doi.org/10.1021/nl5011977 | *Nano Lett.* 2014, 14, 4951–4958

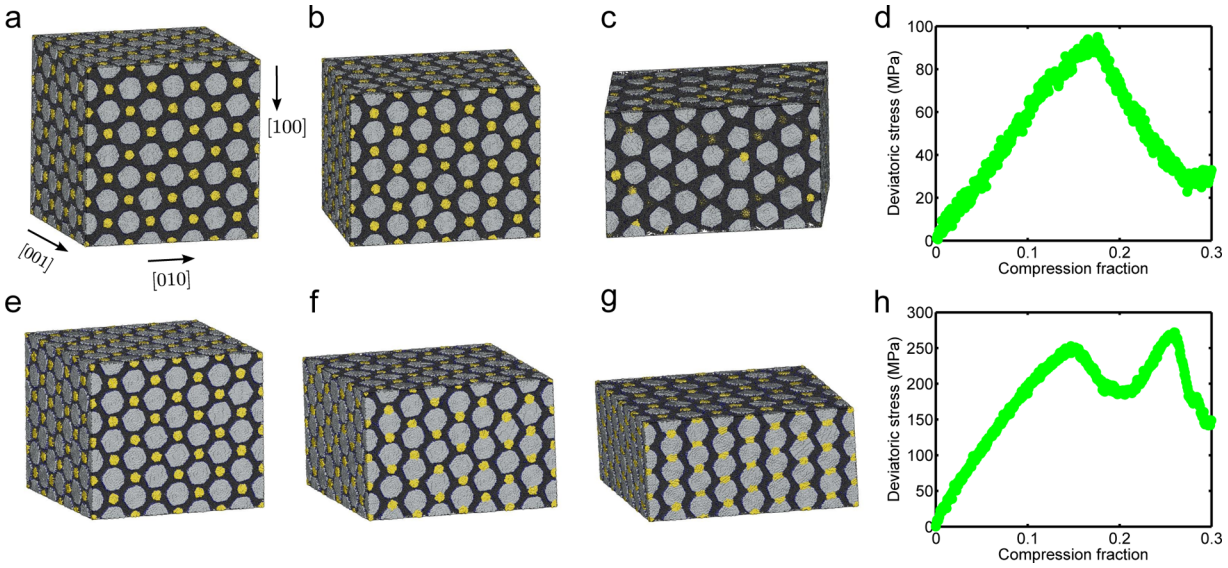

Figure 4. Stress-driven fusion of Ag−Au binary NPSL in NaCl-type superstructure. (a−c) MD simulation snapshots showing the structural evolution of the system deformed at zero external pressure along the [100] direction. (a) The configuration of the system before uniaxial deformation. The silver nanocrystals are colored in silver, and the gold nanocrystals are colored in gold. The black region between the nanocrystals contains thiol molecules adsorbed on the nanocrystal surfaces. (b,c) Configurations at strain equal to −0.15 and −0.3, respectively. (d) Stress−strain curve associated with the deformation at zero external pressure. The yield stress is around 90 MPa. (e−g) Structural evolution of the binary NPSL deformed along the [100] direction in the presence of 500 MPa pressure. Multijunction nanowire array consists of periodic domains of gold and silver nanocrystals are formed at the end of deformation. (h) Stress−strain curve associated with the deformation at 500 MPa pressure. The critical deviatoric stress to induce fusion is around 280 MPa.

three cases, ordered fusion could not be observed (Supplementary Movies S4−S6). This is because with $C_{44}(P = 0) = 68$ MPa, τ of hundreds of MPa would exceed the ideal shear strength[21] and thus the plastic yield strength $\tau_Y(P = 0)$ of the supercrystal, which will trigger supercrystal plasticity before fusion can happen. A moderate pressure $P > 0$ is needed so $\tau_Y(P > 0)$ is enhanced, delaying the competing supercrystal plasticity processes.

This idea motivates us to map out the pressure-dependent fusion behavior of [110] oriented gold NPSLs. We simulate the uniaxial deformation of [110] oriented gold NPSLs under different pressures and look at the configuration of the system at the end of deformation. The system, which is initially equilibrated at a given pressure P, is deformed along the z dimension of the simulation box corresponding the [110] direction, during which the σ_{xx} and σ_{yy} of the ensemble are fixed at P. The shear stress components of the ensemble, σ_{xy}, σ_{xz}, and σ_{yz}, are controlled by barostat to be zero. When P is small, uniaxial compression leads to twinning-like plastic deformation of the superlattice along the [110] direction when the strain reaches around −0.2 (Supplementary Movie S6). This triggers mechanical yielding of the system. Further deformation leads to partial structural disordering of the superlattice. When P is increased to around 100 MPa, partial fusion of nanoparticles along the [110] direction starts to emerge (Supplementary Movie S7). If P is further increased, more and more nanoparticles are fused together along the [110] direction before the system mechanically yields. Finally, when P reaches 350 MPa, all the nanoparticles are able to fuse together along the [110] direction. This transition is shown in the simulation snapshots of Figure 3a−c and Supplementary Figure S2. Such simulation over a wide range of pressure P enables us to plot a nonequilibrium stress-driven "processing diagram" of the [110] oriented gold NPSLs, which is presented in Figure 3d. The processing diagram indicates the existence of three regions in stress space, corresponding to viscoelasticiy, partial fusion, and formation of ordered nanowire arrays, respectively. Formation of nanowire arrays only happens when both the pressure P and the deviatoric stress $\tau \equiv \sigma_{zz} - P$ exceed certain critical values. The critical fusion pressure is found to be $P_{fusion} \approx 350$ MPa, and the critical fusion deviatoric stress is found to be $\tau_{fusion} \approx 170$ MPa.

We have also studied stress driven fusion of gold NPSLs consisting of larger-sized gold nanoparticles and found the same order of magnitude of critical pressure and deviatoric stress values. For gold NPSLs consisting of dodecanethiol ($S(CH_2)_{11}CH_3$) passivated gold nanocrystals with core diameter ~4 nm in *fcc* type superstructure, the critical pressure P_{fusion} and deviatoric stress τ_{fusion} needed for formation of nanowire arrays are both found to be around 200 MPa.

While stress-driven fusion of single-component gold NPSLs have been demonstrated in experiments,[2,9] stress-driven fusion of binary NPSLs[2] has not been shown experimentally. We hence carried out MD simulation of a model binary NPSL, Ag−Au binary NPSL in sodium chloride (NaCl)-type superstructure. Binary NPSLs with this type of supercrystal structure have been created experimentally.[2,22] Previous studies demonstrated that the structure of binary NPSLs depends on the size ratio of small and large nanoparticles, $\gamma = R_{small}/R_{large}$.[23,24] The icosahedron-shape gold nanocrystal in our Ag−Au binary NPSL has diameter around 2 nm, containing 309 gold atoms. The silver nanocrystal has diameter around 5 nm and contains 3871 silver atoms. This gives $\gamma \approx 0.4$, which is very close to the most stable value for NaCl-type structure.[22] The gold and silver nanocrystals are both fully passivated by octanethiol ligands. The simulation system, shown in Figure 4a is a 4 × 4 × 4 supercell, containing 256 silver nanoparticles and 256 gold nanoparticles. The simulation set up and procedures for stress-driven fusion of the binary NPSL are similar to those for gold NPSLs discussed earlier.

dx.doi.org/10.1021/nl5011977 | *Nano Lett.* 2014, 14, 4951−4958

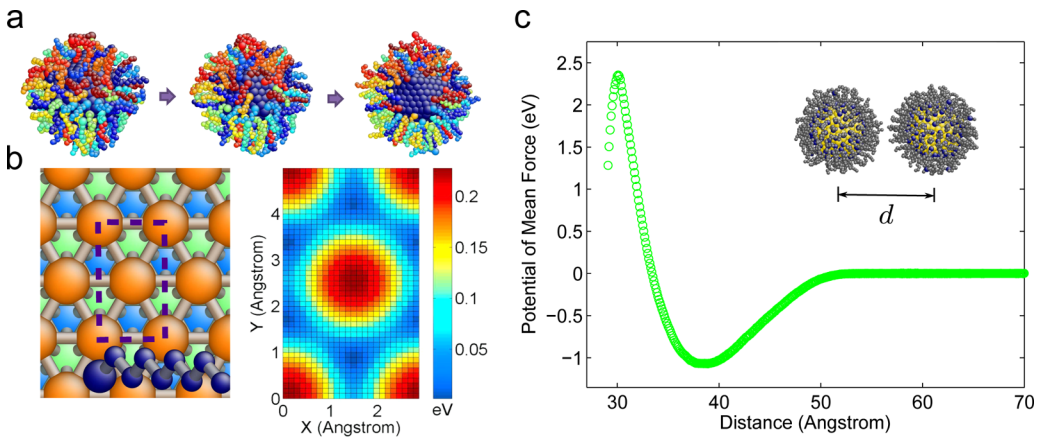

Figure 5. (a) Simulation snapshots of ligands being displaced from the contact region between two nanoparticles during stress-driven fusion. Atoms belonging to the same ligand molecule are colored the same. (b) Surface configuration of the gold nanocrystal in our model and calculated potential energy surface for moving a ligand on the surface. In the left panel of b, the top surface layer of the nanocrystal is colored in orange, which is shown together with the two layers beneath (green and blue). A thiol molecule is also depicted in the figure. The dashed box represents the region for potential energy surface calculation, the result of which is shown in the right panel of b. (c) Calculated potential of mean force as a function of distance between two nanoparticles. The potential of mean force reaches its maximum shortly before the fusion of two nanoparticles.

Figure 4a–d shows that, if we deform the binary NPSL along the [100] direction of the superlattice under $P = 0$, no ordered fusion of nanoparticles occurs. The system mechanically yields at around $\tau_Y = 90$ MPa before the gold and silver nanocrystal cores were able to jam together to form contact. Accompanied with this yielding, the smaller-sized gold nanoparticles are displaced from their lattice sites along the [100] direction, which is the nearest-neighbor direction in NaCl-type superlattice (Supplementary Movie S8). In contrast, when the binary NPSL is deformed in the presence of $P = 500$ MPa, the system is superstructurally stiffer, and the nanoparticles remain jammed in their lattice sites during deformation. This pressure-induced increase in yield strength $\tau_Y(P > 0) > \tau_Y(P = 0)$, so-called Mohr–Coulomb[25] or non-Schmid yield shown in Figure 4e–h, allows the uniaxial stress to rise high enough to drive the fusion of silver and gold nanoparticles along the [100] direction, forming Ag–Au multijunction nanowire arrays (Supplementary Movie S9).

Our simulations of gold NPSLs and Ag–Au binary NPSLs reveal that a few conditions need to be met simultaneously for ordered fusion of nanoparticles in these NPSLs: (a) the presence of a pressure background of more than several hundred MPa. The presence of a moderately high pressure P on the supercrystal, $P > 0.2B$, increases its uniaxial yield strength τ_Y significantly (Figure 3d). The computed finite-pressure elastic constants C_{11}, C_{12}, and C_{44} of the gold NPSLs also increase significantly (Figure 3e). When the mechanical strength of the system is increased such that the yielding deviatoric stress becomes larger than the critical fusion deviatoric stress, $\tau_Y(P) > \tau_{fusion}(P)$, ordered fusion of NPSL can happen. (b) The applied deviatoric stress needs to be larger than the critical fusion deviatoric stress, $\tau > \tau_{fusion}$. It can be seen from Figure 3d that if the deviatoric stress has not reached the critical value, the system is still in the viscoelasticity regime. Physically, neighboring nanoparticles have not come close enough to enable the contact formation of the nanocrystal cores. (c) Right alignment of the deviatoric stress with respect to the crystallographic direction of the superlattice. Our simulation indicates that proper alignment of deviatoric stress ensures ordered nanoparticle fusion. Formation of nanowire array is found to occur when the deviatoric stress aligns with the nearest-neighbor direction of nanoparticles in NPSLs.

If the fusion criterion is $\tau_Y(P) > \tau > \tau_{fusion}(P)$, what then controls τ_{fusion}? At the molecular level, the mechanism of nanoparticle fusion is deviatoric stress induced ligand displacement on nanocrystal surface, which depassivates the gold nanocrystals locally and allows them to form direct metal–metal contact (grain boundary) and fuse together. The ligands between neighboring nanocrystals along the deviatoric stress direction sustain higher local pressure than ligands elsewhere on the surface, creating a chemical potential gradient for ligand surface diffusion. It has been shown recently[26,27] that surface diffusion on sub-10 nm metallic nanoparticles is so active at room temperature that it can support Coble creep. The large surface curvature of nanocrystal facilitates ligand surface diffusion, as the free volume per ligand is higher on surfaces with higher curvature.[28] If the nanoparticles are continuously pushed toward each other, ligands will eventually leave the contact region (ligand source) to regions of less local pressure (ligand sink), followed by the fusion of gold nanocrystal. This ligand source-to-ligand sink process by surface diffusion is shown in the simulation snapshots of Figure 5a. The possibility of ligands being displaced by mechanical force on gold surfaces had been unequivocally demonstrated by Liu et al.,[29] where they found the tip of AFM can displace self-assembled thiol layers on gold surfaces above a critical contact pressure around 1 GPa.[30] Because of the aforementioned curvature effects, the critical contact pressure for displacing ligands on nanocrystal surface should be lower, which in our study was found to be several hundred MPa. The calculated potential energy barrier Q for displacing of an single ligand on gold (111) surface is around 50 meV in our simulation (Figure 5b), a value that agrees with first-principles calculated thiol diffusion barrier on gold (111) surface.[31] This low energy barrier at $P = 0$ means such surface migration can indeed happen at room temperature.[32]

The critical deviatoric stress for fusion of NPSL can be estimated by calculating the free energy barrier of fusion between two individual nanoparticles. The potential of mean force (PMF) between two nanoparticles can be calculated via steered molecular dynamics (SMD).[12] On the basis of

dx.doi.org/10.1021/nl5011977 | Nano Lett. 2014, 14, 4951–4958

Jarzynski's equality,[33] PMF reflects the free energy difference between the initial and final states during a nonequilibrium process. During our SMD calculation of PMF, two individual gold nanoparticles, initially separated over a distance of 150 Å, are coupled together by a fictitious spring and pulled toward each other with a constant pulling velocity equal to 0.1 Å per picosecond. This pulling speed, when translated into engineering strain rate of deformation, is close to the strain rate we used for stress-driven fusion simulation. The nanoparticles are allowed to rotate freely about their centers of mass during the SMD pulling process. The final PMF is the average of six independent trajectories along the same pulling path. Figure 5c shows the calculated PMF. The PMF has a well-defined potential minimum where entropic repulsion between the ligands balances the van der Waals enthalpic attraction. The PMF also has a steep repulsive region, the maximum of which corresponds to the "fusion distance"[12] between two nanoparticles. Two nanoparticles will fuse together when their distance is smaller than the fusion distance. From the computed PMF, the fusion free energy barrier between two nanoparticles is determined to be ΔF = 3.5 eV. This number can be approximated as the free energy barrier of fusion per nanoparticle in the gold NPSL. We can then estimate the minimum deviatoric stress based on the thermodynamic principle that work done on the system must be larger than the free energy change. Assuming the linear stress−strain relationship, the net work done on the NPSL per particle before fusion is $w = \tau_{\text{fusion}}\varepsilon_c\Omega/2$, where ε_c is the critical fusion strain and Ω the volume per nanoparticle in the NPSL. We then reach the following inequality:

$$\frac{1}{2}\tau_{\text{fusion}}\varepsilon_c\Omega > \Delta F$$

Using the numbers from the simulation, $\varepsilon_c \approx 0.2$ (Supplementary Figure S2) and $\Omega \approx 4.5 \times 10^4$ Å^3 (Figure 1b), we calculate the critical deviatoric stress $\tau_{\text{fusion}} > 120$ MPa. This number is close to the critical deviatoric stress obtained from the fusion processing diagram Figure 3d (170 MPa). The success of this "independent particle" model suggests that at critical fusion compression τ_{fusion}, many-body effects on the fusion of a nanoparticle in the NPSL are still relatively minor.

We would like to point out that, while we conclude from our simulations that stress-driven fusion of gold NPSLs require pressure and deviatoric stress of order several hundred MPa, these critical values are obtained from simulations with very high strain rate of deformation and very small simulation supercell, thereby may not necessarily reflect the minimum critical stress values to achieve fusion in laboratory experiments with much lower strain rate. Because of the time-scale limit of MD simulation, strain rates in MD simulation are typically very high, ranging from 10^{-1} to 10^{-5} per picosecond. The strain rate of deformation in our simulation (-1.0×10^{-4} per picosecond) is a common value for MD simulation but still many orders of magnitude higher than common experimental strain rate. We have carried out preliminary studies on the effects of strain rate on the critical fusion deviatoric stress and found lower stress value when strain rate is reduced. This is not surprising considering the NPSLs are viscoelastic. Therefore, the experimental critical fusion pressure and deviatoric stresses could be lower than the values obtained by our simulation, if the interatomic potentials used in our simulation are sufficiently accurate. We also emphasize that the critical fusion deviatoric stress is not the stress to realize the sintering of bare, unpassivated gold nanocrystals. Instead, the majority of the load in stress-driven fusion was the flow stress to deform and replace the passivating ligands absorbed on the nanocrystal surfaces. Once the ligands are displaced, sintering of gold nanocrystals can happen with much lower applied load. Indeed, Lu et al. demonstrated that cold welding of gold nanowires can occur with contact pressure less than a few MPa at room temperature.[34]

A potentially important implication of our simulation is that stress-driven fusion of NPSLs may only require pressure and deviatoric stress of an order several hundred MPa or even lower, in which case special pressure-generating devices such as diamond anvil cell may not be necessary. In Wu et al.'s high pressure experiment,[8] formation of gold nanowire arrays from gold NPSLs occurs at pressure above 10 GPa. This is because the deviatoric stress in their experiment is generated only when the pressure transmitting medium (PTM), namely, silicone oil, is solidified in that range of pressure. Yet solidification of PTM is not the only way to generate deviatoric stress. One can directly compress a NPSL sample immersed in a PTM to induce deviatoric stress on top of a compressive pressure. Indeed, hydraulic compression machines, capable of generating axial deviatoric stress while maintaining radial pressure up to 400 MPa, have been used to study the phase transformation of zirconia.[35] Such instruments are clearly more suitable than diamond anvil cell should stress-driven fusion of NPSLs become a viable route for large-scale synthesis of nanowire arrays.

To summarize, we have studied the mechanical response and stress-driven fusion of gold NPSLs and Ag−Au binary NPSLs. We study the conditions under which ordered nanowire array can be formed via stress-driven fusion and present molecular-level understanding of the fusion process. First, deviatoric (uniaxial) stress τ_{fusion} of hundreds of MPa is needed to set up ligand source−sink mass action on the surface of the same nanoparticle, with sufficient chemical potential gradient to drive surface diffusion, which is certainly facile enough at room temperature ($Q \approx 50$ meV) if the pressure is not exceedingly high. Second, moderate hydrostatic (triaxial) pressure $P \approx 0.2B(P = 0)$ is necessary to elevate the supercrystal yield strength τ_Y significantly. This is because the applied deviatoric stress can also be relaxed by superstructural plasticity (dislocation, twinning, phase transformation, etc.) of the supercrystal, and if these processes happen before fusion, it will be difficult to have ordered fusion. These conditions are summarized in a single equation $\tau_Y(P) > \tau > \tau_{\text{fusion}}(P)$, and we have given numerical estimates of both $\tau_Y(P)$ and $\tau_{\text{fusion}}(P)$ in this letter, $\tau_Y(P)$ by Mohr−Coulomb type of calculation and $\tau_{\text{fusion}}(P)$ by molecular level energy estimates, and direct calculations. On the basis of these understandings we have constructed a room-temperature processing diagram (Figure 3d) that is shown to be effective for both Au and Ag−Au NPSLs. Our study suggests that stress-driven fusion could potentially be employed to create novel nanostructures, such as multijunction nanowire arrays, in a scalable and cost-effective way. This is an exciting opportunity considering the structural richness and compositional tunability that can be achieved in binary and multicomponent NPSLs.[2,36] Because both τ and P required are rather low (several hundred MPa), it should then be entirely possible that stress-driven fusion of binary NPSLs could be used for industrial-scale production of multijunction nanowire arrays, for use in bulk-scale applications such as photovoltaics[37,38] and catalysis.

dx.doi.org/10.1021/nl5011977 | Nano Lett. 2014, 14, 4951−4958

■ ASSOCIATED CONTENT

Supporting Information

Detailed simulation methods, including interaction potential models and simulation procedures; discussions on ligand conformation change and displacement on nanocrystal surface during stress-driven fusion; stress−strain curves and final molecular configurations of stress-driven fusion under different hydrostatic pressure; methods for computing the elastic constants of nanoparticle superlattice; supplementary Figure S1−S3 and supplementary Movies S1−S9. This material is available free of charge via the Internet at http://pubs.acs.org.

■ AUTHOR INFORMATION

Corresponding Author

*(J.L.) E-mail: liju@mit.edu.

Notes

The authors declare no competing financial interest.

■ ACKNOWLEDGMENTS

We thank Huimeng Wu for very helpful discussions. W.L. and J.L. acknowledge support by NSF under Grant No. DMR-1120901. H.F. thanks U.S. Department of Energy, Office of Basic Energy Sciences, Division of Materials Sciences and Engineering. Sandia is a multiprogram laboratory operated by Sandia Corporation, a wholly owned subsidiary of Lockheed Martin Corporation, for the U.S. Department of Energy's National Nuclear Security Administration under Contract DEAC0494AL85000. Computational time on the Extreme Science and Engineering Discovery Environment (XSEDE) under the grant number TG-DMR130038 is gratefully acknowledged.

■ REFERENCES

(1) Talapin, D. V.; Lee, J.-S.; Kovalenko, M. V.; Shevchenko, E. V. *Chem. Rev.* **2010**, *110*, 389−458.
(2) Shevchenko, E. V.; Talapin, D. V.; Kotov, N. A.; O'Brien, S.; Murray, C. B. *Nature* **2006**, *439*, 55−59.
(3) Lee, D.; Jia, S.; Banerjee, S.; Bevk, J.; Herman, I.; Kysar, J. *Phys. Rev. Lett.* **2007**, *98*, 026103.
(4) Mueggenburg, K. E.; Lin, X.-M.; Goldsmith, R. H.; Jaeger, H. M. *Nat. Mater.* **2007**, *6*, 656−660.
(5) Tam, E.; Podsiadlo, P.; Shevchenko, E.; Ogletree, D. F.; Delplancke-Ogletree, M. P.; Ashby, P. D. *Nano Lett.* **2010**, *10*, 2363−2367.
(6) Podsiadlo, P.; Krylova, G.; Lee, B.; Critchley, K.; Gosztola, D. J.; Talapin, D. V.; Ashby, P. D.; Shevchenko, E. V. *J. Am. Chem. Soc.* **2010**, *132*, 8953−8960.
(7) Yan, C.; Arfaoui, I.; Goubet, N.; Pileni, M.-P. *Adv. Funct. Mater.* **2013**, *23*, 2315−2321.
(8) Wu, H.; Bai, F.; Sun, Z.; Haddad, R. E.; Boye, D. M.; Wang, Z.; Fan, H. *Angew. Chem., Int. Ed.* **2010**, *49*, 8431−8434.
(9) Wu, H.; Bai, F.; Sun, Z.; Haddad, R. E.; Boye, D. M.; Wang, Z.; Huang, J. Y.; Fan, H. *J. Am. Chem. Soc.* **2010**, *132*, 12826−12828.
(10) Wang, Z.; Schliehe, C.; Wang, T.; Nagaoka, Y.; Cao, Y. C.; Bassett, W. A.; Wu, H.; Fan, H.; Weller, H. *J. Am. Chem. Soc.* **2011**, *133*, 14484−14487.
(11) Landman, U.; Luedtke, W. D. *Faraday Discuss.* **2004**, *125*, 1−22.
(12) Schapotschnikow, P.; Pool, R.; Vlugt, T. J. H. *Nano Lett.* **2008**, *8*, 2930−2934.
(13) Parrinello, M.; Rahman, A. *Phys. Rev. Lett.* **1980**, *45*, 1196−1199.
(14) Parrinello, M.; Rahman, A. *J. Appl. Phys.* **1981**, *52*, 7182−7190.
(15) Parrinello, M.; Rahman, A. *J. Chem. Phys.* **1982**, *76*, 2662−2666.
(16) Ray, J. R. *Comput. Phys. Rep.* **1988**, *8*, 109−151.
(17) Foiles, S. M.; Baskes, M. I.; Daw, M. S. *Phys. Rev. B* **1986**, *33*, 7983−7991.
(18) Shinoda, W.; Shiga, M.; Mikami, M. *Phys. Rev. B* **2004**, *69*, 134103.
(19) Martyna, G. J.; Tobias, D. J.; Klein, M. L. *J. Chem. Phys.* **1994**, *101*, 4177−4189.
(20) Podsiadlo, P.; Lee, B.; Prakapenka, V. B.; Krylova, G. V.; Schaller, R. D.; Demortiere, A.; Shevchenko, E. V. *Nano Lett.* **2011**, *11*, 579−588.
(21) Zhu, T.; Li, J. *Prog. Mater. Sci.* **2010**, *55*, 710−757.
(22) Saunders, A. E.; Korgel, B. A. *ChemPhysChem* **2005**, *6*, 61−65.
(23) Redl, F. X.; Cho, K. S.; Murray, C. B.; O'Brien, S. *Nature* **2003**, *423*, 968−971.
(24) Murray, M. J.; Sanders, J. V. *Philos. Mag. A* **1980**, *42*, 721−740.
(25) Schuh, C. A.; Lund, A. C. *Nat. Mater.* **2003**, *2*, 449−452.
(26) Tian, L.; Li, J.; Sun, J.; Ma, E.; Shan, Z.-W. *Sci. Rep.* **2013**, *3*, 2113.
(27) Sun, J.; He, L. B.; Lo, Y.-C.; Sun, L. T.; Xu, T.; Bi, H. C.; Zhang, Z.; Mao, S.; Li, J. Submitted for publication.
(28) Lane, J. M. D.; Grest, G. S. *Phys. Rev. Lett.* **2010**, *104*, 235501.
(29) Liu, G. Y.; Salmeron, M. B. *Langmuir* **1994**, *10*, 367−370.
(30) Salmeron, M. *Tribol. Lett.* **2001**, *10*, 69−79.
(31) Beardmore, K. M.; Kress, J. D.; Gronbech-Jensen, N.; Bishop, A. R. *Chem. Phys. Lett.* **1998**, *286*, 40−45.
(32) Sheehan, P.; Whitman, L. *Phys. Rev. Lett.* **2002**, *88*, 156104.
(33) Jarzynski, C. *Phys. Rev. Lett.* **1997**, *78*, 2690−2693.
(34) Lu, Y.; Huang, J. Y.; Wang, C.; Sun, S.; Lou, J. *Nat. Nanotechnol.* **2010**, *5*, 218−224.
(35) Chen, I. W.; Morel, P. *J. Am. Ceram. Soc.* **1986**, *69*, 181−189.
(36) Dong, A.; Chen, J.; Vora, P. M.; Kikkawa, J. M.; Murray, C. B. *Nature* **2010**, *466*, 474−477.
(37) Milliron, D. J.; Hughes, S. M.; Cui, Y.; Manna, L.; Li, J. B.; Wang, L. W.; Alivisatos, A. P. *Nature* **2004**, *430*, 190−195.
(38) Wallentin, J.; Anttu, N.; Asoli, D.; Huffman, M.; Åberg, I.; Magnusson, M. H.; Siefer, G.; Fuss-Kailuweit, P.; Dimroth, F.; Witzigmann, B.; Xu, H. Q.; Samuelson, L.; Deppert, K.; Borgstrom, M. T. *Science* **2013**, *339*, 1057−1060.

Deviatoric Stress-Driven Fusion of Nanoparticle Superlattices
Supplementary Information

Wenbin Li,[1] Hongyou Fan,[2] and Ju Li[3,1]

[1]*Department of Materials Science and Engineering,*
Massachusetts Institute of Technology,
Cambridge, Massachusetts 02139, USA

[2]*Sandia National Laboratories, Advanced Materials Laboratory,*
1001 University Boulevard SE, Albuquerque, New Mexico 87106, USA

[3]*Department of Nuclear Science and Engineering,*
Massachusetts Institute of Technology,
Cambridge, Massachusetts 02139, USA

I. SIMULATION METHODS

The MD simulations reported in the paper employ the LAMMPS code [1]. Periodic boundary conditions are always used. The timestep for integration of equation of motion is set to be 1.0 fs. For stress-driven fusion simulation, the simulation system typically involves around 2500 gold nanoparticles (∼5 million atoms). To save computational resources, the fusion processing diagram for [110] oriented gold NPSLs (Fig. 3d in the main text) was mapped out using a system containing 192 nanoparticles. We have checked the system size effect and found the results for large and small simulation systems agree with each other well. A set of well-annotated programs used by us to generate the LAMMPS input files for simulation of individual ligand-passivated gold nanoparticles and NPSLs are freely available on github.com at `https://github.com/liwenbin/superlattice`.

A. Intermolecular Potential Models

The assignment of interaction potential is a critical issue in MD simulation. In our simulation, Morse potential was chosen to describe the interaction between gold atoms [2, 3]. Although embedded-atom method (EAM) potential [4] is known to be a more accurate potential model for metals, especially for metallic nanostructures, we found in our simulation that EAM potential has a few problems when used together with pair potential description of gold-sulfur interaction. Sulfur atoms tend to cause surface roughening of gold nanocrystals modeled with EAM potential. A small portion of sulfur atoms can penetrate one atomic layer beneath the gold surface, which no experimental evidence is available for support and is unphysical in our belief. This motivates our choice of Morse potential to model gold-gold interaction [2, 3]. While the simulations reported in this paper use Morse potential, we have nevertheless performed extensive simulations using EAM potential. The conclusions drawn in our paper are not qualitatively affected. The critical hydrostatic pressure and deviatoric stress needed for fusion of gold NPSL into gold nanowire array was found to be higher (within a factor of two) for nanocrystals modeled with EAM potential. The higher values can be explained by the aforementioned penetration of sulfur atoms beneath gold nanocrystal surface, which make it more difficult for ligands being displaced from the contact region between two neighboring nanoparticles before fusion.

To describe the interaction of alkanethiol ligands, we use the united atom (UA) potential by Paul *et al* [5]. Kushik *et al*'s recent work [6] demonstrated that Paul *et al*'s UA potential can accurately reproduce the chain conformation and dynamics of ligands modeled by very accurate, but computationally demanding all-atom MM3 potential [7]. The UA potential includes bond, angle, dihedral and non-bonded interactions.

The interaction between thiol ligands and gold nanocrystals is subtle, due to the quantum-mechanical nature of sulfur-gold bonding. The adsorption configuration of thiol on gold surface is still under debate [8]. Most studies in the literature use Morse potential to parameterize gold-sulfur interaction [9–12]. Our gold-sulfur interaction model follows Zhang *et al* [9], except that we use Lennard-Jones potential instead of Morse potential to fit the adsorption energies of sulfur atom on gold surfaces, as Morse potential has a relatively soft core which induces unphysical features at very high pressure. We note that Schapotschnikow *et al* [13] also use Lennard-Jones potential to model gold-sulfur interaction in their simulation of interactions between individual gold nanoparticles. We have selected Zhang *et al*'s gold-sulfur model [9] because the thiol diffusion barrier computed from Zhang *et al*'s model is very close to first-principles calculated thiol diffusion barrier on gold (111) surface assuming direct adsorption geometry [14], as well as gold adatom diffusion barrier on gold (111) surface [15]. The gold adatom model, namely thiol ligands bind to gold surface via gold adatoms, has recently emerged as a strong candidate for ligand adsorption on gold surface [8]. Due to the covalent bonding between sulfur and gold, thiol diffusion on gold surface may involve diffusion of thiol-adatom complex, in which case the thiol diffusion barrier should be close to that of gold adatom. Indeed, fast diffusion of thiol ligands on gold surface was experimentally observed [16], suggesting that the thiol diffusion barrier should be close to thermal energy at room temperature.

For silver-gold (Ag-Au) binary nanoparticle superlattice simulation, we use Morse potential [2] to describe the interaction between the silver atoms. The cross-interaction between gold and silver atoms are computed using Lorentz-Berthelot mixing rules. As previous studies showed that the interaction strength and equilibrium distance of Ag-S bond is very close to those of Au-S bond [17, 18], we use the Au-S interaction parameters to approximate those of Ag-S interaction. The non-bonded interactions between the alkyl group of thiol ligands and silver are relatively weak. Small variation of these interaction parameters is unlikely to influence the simulation results much. Hence, the parameters are taken to be same as those

between ligands and gold nanoparticles.

The force field parameters for the interaction models described above are listed in details bellow.

1. *Gold-gold interaction*

$$E = D_0 \left[e^{-2\alpha(r-r_0)} - 2e^{-\alpha(r-r_0)} \right], \qquad r < r_c \tag{1}$$

where $D_0 = 10.956$ kcal/mol, $\alpha = 1.5830$ Å^{-1}, $r_0 = 3.0242$ Å. The interaction cut-off distance $r_c = 10$ Å is the default value for non-bonded interactions in our simulations. Interaction potentials are shifted to zero at r_c.

2. *Ligand intra- and inter-molecular interactions*

The thiol ligands ($S(CH_2)_nCH_3$) are coarse-grained such that each CH_2 or CH_3 unit is treated as a single atom. The total conformation energy of thiol molecules consists of energy coming from bond-stretching, angle-bending, dihedral-torsion, and non-bonded interactions.

$$E = E_{bond} + E_{angle} + E_{torsion} + E_{non-bonded} \tag{2}$$

where

$$E_{bond} = k(r - r_0)^2 \tag{3}$$

$$E_{angle} = k' \left[\cos(\theta) - \cos(\theta_0) \right]^2 \tag{4}$$

$$E_{dihedral} = \frac{1}{2}K_1 \left[1 + \cos(\phi)\right] + \frac{1}{2}K_2 \left[1 - \cos(2\phi)\right] + \frac{1}{2}K_3 \left[1 + \cos(3\phi)\right] \tag{5}$$

$$E_{non-bonded} = 4\epsilon \left[\left(\frac{\sigma}{r}\right)^{12} - \left(\frac{\sigma}{r}\right)^{6} \right], \qquad r < r_c \tag{6}$$

The interaction parameters for the alkyl groups of thiol ligands are the original values of Paul *et al* [5, 6]. Interactions parameters involving sulfur were taken from literature [12, 19–21]. The interaction parameters are listed in Table I.

For non-bonded interactions, the standard Lorentz-Berthelot mixing rules are used to compute the cross-interaction terms.

TABLE I. Interaction Parameters for Ligand Molecules

bond	r_0 (Å)	k [kcal/(mol/Å^2)]	
S-CH_2	1.81	222	
CH_2-CH_2	1.53	317	
CH_2-CH_3	1.53	317	
angle	θ_0 (degree)	k' (kcal/mol)	
S-CH_2-CH_2	114.4	62.5	
CH_2-CH_2-CH_2	110.01	60.0	
CH_2-CH_2-CH_3	110.01	60.0	
dihedral	K_1 (kcal/mol)	K_2 (kcal/mol)	K_3 (kcal/mol)
S-CH_2-CH_2-CH_2	1.6	-0.8670	3.24
CH_2-CH_2-CH_2-CH_2	1.6	-0.8670	3.24
CH_2-CH_2-CH_2-CH_3	1.6	-0.8670	3.24
non-bonded interaction	σ (Å)	ϵ (kcal/mol)	
S	4.25	0.39743	
CH_2	4.009	0.09344	
CH_3	4.009	0.22644	

3. Ligand-gold interaction

The ligand-gold interaction consists of sulfur-gold interaction and alkyl group-gold interaction. The interaction between gold and sulfur is modeled by Lennard-Jonnes potential:

$$E = 4\epsilon \left[\left(\frac{\sigma}{r}\right)^{12} - \left(\frac{\sigma}{r}\right)^{6} \right], \qquad r < r_c \tag{7}$$

where $\epsilon = 3.182$ kcal/mol, $\sigma = 2.586$ Å.

The interaction of alkyl units with gold is modeled by Lennard-Jones potential as well. The interaction strength, however, is much weaker than sulfur-gold interaction. The interaction parameters are taken from literature [12, 19]. For interaction between Au and CH_2 units, $\epsilon = 0.0678$ kcal/mol, $\sigma = 3.42$ Å. For interaction between Au and CH_3 unit, $\epsilon = 0.0826$ kcal/mol, $\sigma = 3.42$ Å.

4. *Interaction parameters for silver-gold binary nanoparticle superlattice*

For silver-gold binary NPSL simulation, we also use Morse potential to describe the interaction between the silver atoms:

$$E = D_0 \left[e^{-2\alpha(r-r_0)} - 2e^{-\alpha(r-r_0)} \right], \qquad r < r_c \tag{8}$$

The interaction parameters, taken from literature [2], are $D_0 = 7.499$ kcal/mol, $\alpha = 1.3535$ Å^{-1}, and $r_0 = 3.1300$ Å. The interaction between gold and silver atoms are computed using Lorentz-Berthelot mixing rules, which gives $D_0 = 9.2275$ kcal/mol, $\alpha = 1.4683$ Å^{-1}, $r_0 = 3.0771$ Å.

For the interaction between the sulfur atoms of thiol ligands and silver nanoparticles, previous studies showed that the interaction strength and equilibrium distance of Ag-S bond are very close to those of Au-S bond [17, 18]. Therefore, the Ag-S interaction parameters are taken to be the same as those of Au-S interation, namely

$$E = 4\epsilon \left[\left(\frac{\sigma}{r}\right)^{12} - \left(\frac{\sigma}{r}\right)^{6} \right], \qquad r < r_c \tag{9}$$

where $\epsilon = 3.182$ kcal/mol, $\sigma = 2.586$ Å.

The van der Waals interaction between the alkyl group of thiol and silver is relatively weak. Small variation of this set of parameters will not influence the simulation results much. Hence, the parameters are taken to be same as those of thiol-gold interaction.

B. Simulation Procedures

1. *Stress-driven fusion simulation*

We first build individual ligand-passivated gold nanoparticles through MD simulation. An icosahedral gold nanocrystal is put at the center of a simulation box, surrounded by of thiol ligands. The number of ligands is larger than the value corresponding to the maximum ligand coverage on nanocrystal surface. The simulation box is large enough so that periodic images do not interact with each other. Initially, the temperature of the system is set to be 450 K in the constant particle number, constant volume and constant temperature (NVT) ensemble. Due to the strong attractive interactions between gold and sulfur atoms, the thiol ligands start to self-assemble on the nanocrystal surface. After running simulation for $\sim$1

ns, the temperature of the system is cooled to 300 K over a period of 1 ns. The system is then allowed to equilibrate at 300 K for more than 3 ns. At the end of simulation, ligands not absorbed on the nanocrystal surface will be removed and the configuration will be used for building nanoparticle superlattice.

To build gold NPSLs, the ligand-passivated gold nanoparticles are initially put at the lattice sites corresponding to *fcc* superlattice. Previous simulation of gold NPSL using different potential models by Landman *et al* suggested that the favorable superlattice structure is controlled by the ratio of ligand length and nanocrystal core size [22]. Our own extensive (more than 20 ns) Parrinello-Rahman MD simulation [23, 24] with variable size and shape of simulation box confirm that *fcc* is indeed the most stable superstructure for the nanoparticle superlattices considered in this work. If the length of ligand is increased or the size of gold core is decreased, we are able to observe *fcc* to body-centered cubic (*bcc*) or body-centered tetragonal (*bct*) structural transitions [22].

The nanoparticles put at the lattice sites of *fcc* superstructure are initially far away from each other, with the distance between two nearest-neighbor nanoparticles around two times the diameter of a nanoparticle. We then put the system under the constant temperature, constant stress (thermodynamic tension), and particle number ($T\mathbf{t}N$) ensemble. Nosé-Hoover type thermostat and barostat [24–27] are used to control temperature and stress, and the simulation box is allowed to change in both size and shape [23, 24]. The damping coefficients for thermostat and barostat are both 0.01 fs^{-1}. Barostat damping coefficient equal to 0.001 fs^{-1} has also been tested but no noticeable difference in simulation results was found. Subsequently, we set the target pressure of the $T\mathbf{t}N$ ensemble to be zero at constant temperature of 300 K, and run simulation for 1 ns. At this stage, the x, y and z dimensions of the simulation box were allowed to shrink or expand independently, but not the xy, yz and xz dimensions. As the barometer couples to the size and shape of simulation box, the nanoparticles would approach each other and the supercrystal becomes compact. In the next step, we allow all dimensions of the simulation box to relax, and equilibrate the superlattice at 300 K and zero stresses in the $T\mathbf{t}N$ ensemble for 2 ns. At the end of this step, the energy and volume of the system would typically have converged.

To study stress-driven fusion of nanoparticle superlattices under different pressure, we first build gold NPSLs with the one of the low-index superlattice direction, namely the [100], [110] or [111] direction, orienting along, for example, the z direction of the orthorhombic

simulation box in Cartesian geometry. We then equilibrate the system in the $T\mathbf{t}N$ ensemble with zero stress components according to the procedures described above. Afterward, the xx, yy and zz stress components of the ensemble (σ_{xx}, σ_{yy} and σ_{zz}) are elevated to the target pressure P over a 1 ns simulation, while σ_{xy}, σ_{yz} and σ_{xz} are fixed at zero. Subsequently, we equilibrate the system under stress components $\sigma_{xx} = \sigma_{yy} = \sigma_{zz} = P$ and $\sigma_{xy} = \sigma_{yz} = \sigma_{xz} = 0$ for 2 ns, followed by uniaxial deformation of the NPSLs. We deform the z dimension of the simulation box (corresponding to one of the low-index superlattice direction) with a fixed engineering strain rate of -1.0×10^{-4} per ps. The length of simulation box dimension along the z direction will be one half of the original length after 5 ns simulation. During deformation, barostat controls the stress components to simulate the uniaxial deformation of the NPSLs in the presence of fluid-generated pressure background. For example, if we deform along the z direction of the simulation box, σ_{xx} and σ_{yy} will be fixed at P, while σ_{xy}, σ_{yz} and σ_{xz} are all controlled to be zero.

The simulation procedures for equilibration and stress-driven fusion of binary NPSLs are similar to single component gold NPSLs.

II. LIGAND CONFORMATION CHANGE AND DISPLACEMENT ON NANOCRYSTAL SURFACES DURING STRESS-DRIVEN FUSION

We have studied the conformation change and displacement of ligands on nanocrystal surfaces during stress-driven fusion along the [110] direction of gold NPSLs at 1 GPa pressure. To measure the ligand conformation change, we calculate the angle between ligand end-to-end vector and the unit vector along the deformation direction, as schematically shown in Fig. S1(a). The end-to-end vector for the i-th ligand is defined as $\vec{h}_i = \vec{r}_{i,\mathrm{CH_3}} - \vec{r}_{i,\mathrm{S}}$, where $\vec{r}_{i,\mathrm{CH_3}}$ and $\vec{r}_{i,\mathrm{S}}$ denote the coordinates of the outmost CH_3 structural unit and the sulfur atom, respectively. Defining $\hat{z}$ to be the unit vector along the deformation direction, the angle between $\vec{h}_i$ and $\hat{z}$ is then calculated as $\theta^i = \arccos\left(\vec{h}_i \cdot \hat{z}/|\vec{h}_i|\right)$. The change of θ^i during deformation would reflect the rotation of the ligand with respect to the deformation direction. We calculate the angle for all ligands in the system at strain zero and strain equal to -0.2, and plot their distributions in Fig. S1(b). It can be seen from the figure that the distribution, centered at 90 degree, becomes narrower when strain goes from zero to -0.2. This indicates that the ligands are being pushed away from the deformation direction.

In Fig. S1(c), we illustrate the measure of ligand displacement on nanocrystal surface. $\vec{d}_i$ is defined to be the vector going from the center of a nanoparticle, on which the i-th ligands is adsorbed, to the sulfur atom of that ligand. The location of sulfur atom is considered to be the binding site of the ligand. The projection of $\vec{d}_i$ along the deformation direction $\hat{z}$, written as $d_i^{||}$, can be calculated as $d_i^{||} = \vec{d}_i \cdot \hat{z}$. $d^{||}$ gives information about the adsorption site of a ligand with respect to the center of nanocrystal along the deformation direction. The distributions of $d^{||}$ for all ligands at strain zero and strain equal to -0.2 are shown in Fig. S1(d). We can see that from strain zero to strain equal to -0.2, fewer ligands have adsorption sites near the "south and north poles" of nanocrystals, where ligands are subjected to deformation directly. Simultaneously, more ligands adopt adsorption sites near the "equators" of nanocrystals. This clearly indicates that ligands are being displaced from the contact regions between two nanoparticles along the deformation direction.

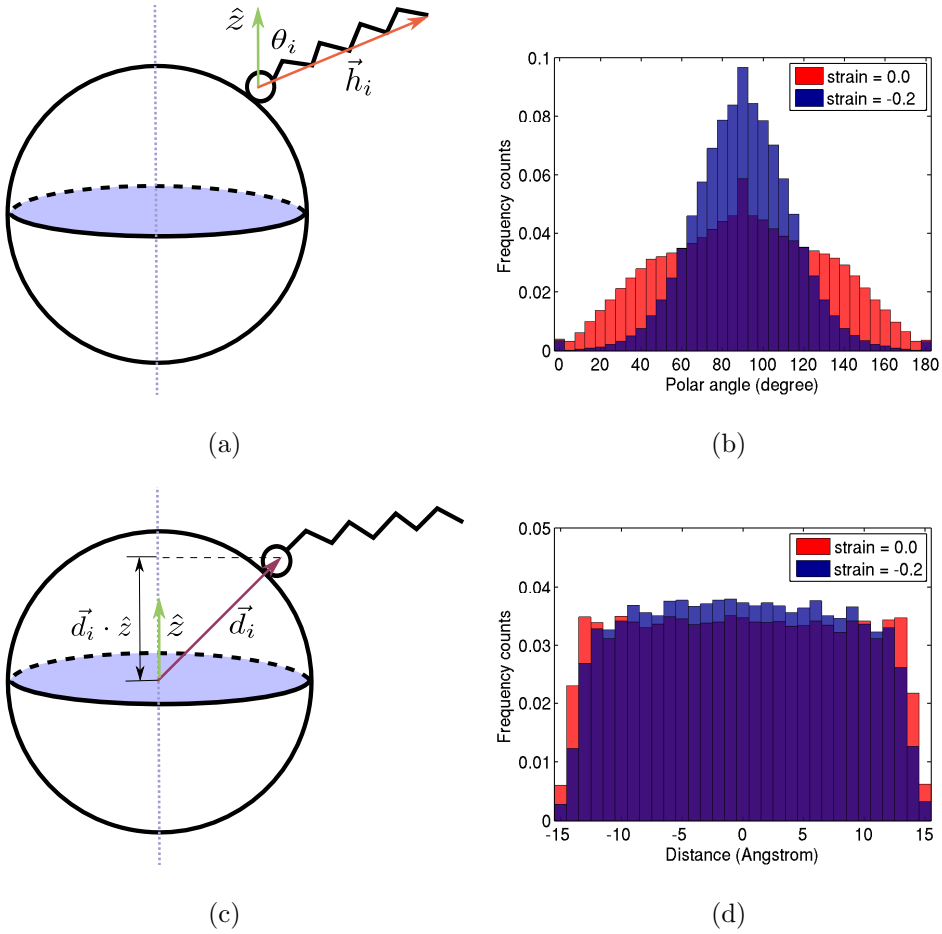

FIG. S1. **Conformation change and displacement of ligands on nanocrystal surface during stress-driven fusion of gold NPSLs along the [110] direction of *fcc* superlattice at 1 GPa pressure.** (a) Schematic of a ligand adsorbed on the surface of a gold nanocrystal. $\hat{z}$ denotes the unit vector along the direction of uniaxial deformation. $\vec{h}_i$ is the end-to-end vector for the i-th ligand; θ^i denotes the angle between $\hat{z}$ and $\vec{h}_i$. Note the actual shape of the gold nanocrystals is icosahedral, not spherical as we schematically draw here. (b) The distribution of angle θ for all ligands at strain $\varepsilon = 0$ and $\varepsilon = -0.2$. The red region belongs only to $\varepsilon = 0$, while the blue region belongs only to $\varepsilon = -0.2$. The purple region is the overlap between two distributions. (c) Illustration of quantities defined for studying ligand displacement on nanocrystal surface. $\vec{d}_i$ is the vector from the center of a nanoparticle to the adsorption site of a ligand adsorbed on it. The dot product between $\vec{d}_i$ and the unit vector $\hat{z}$, written as $\vec{d}_i^{\,||} = \vec{d}_i \cdot \hat{z}$, is a measure of the location of binding site with respect to the center of nanocrystal along the deformation direction. (d) Distributions of $\vec{d}^{\,||}$ calculated for all ligands at $\varepsilon = 0$ and $\varepsilon = -0.2$.

III. DEVIATORIC STRESS VERSUS ENGINEERING STRAIN CURVES AND FINAL MOLECULAR CONFIGURATIONS OF STRESS-DRIVEN FUSION UNDER DIFFERENT PRESSURE

We present here the deviatoric stress versus engineering strain curves and final molecular configurations of the system for gold NPSLs deformed along the [110] direction of *fcc* superlattice under different pressure P. The system contains 192 $Au_{561}(SC_8)_{136}$ gold nanoparticles. We plot the deviatoric stress as a function of compression fraction, which is defined as the absolute value of engineering strain. We also show the corresponding molecular configuration of the system at compression fraction equal to 0.4, at which value we can determine whether ordered gold nanowires are formed. We performed a series of simulation for pressure going from zero to 1 GPa. Below we show the simulation results for $P = 1$ MPa, 10 MPa, 100 MPa, 300 MPa, and 500 MPa.

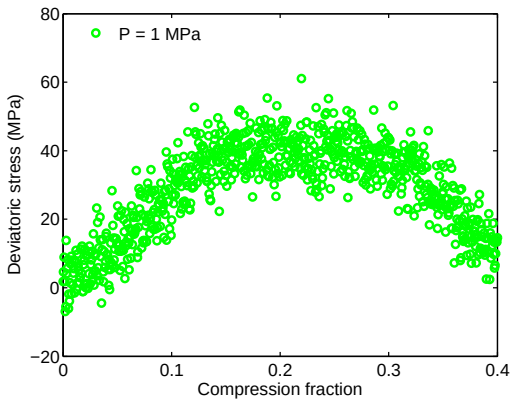

(a)

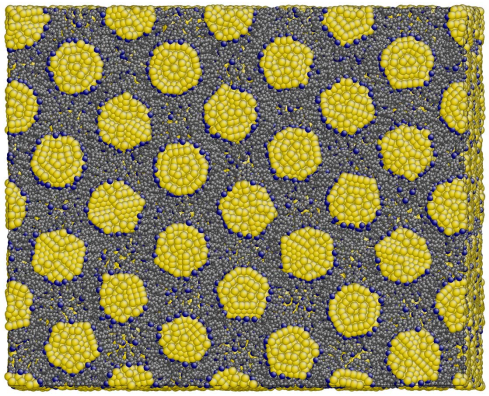

(b)

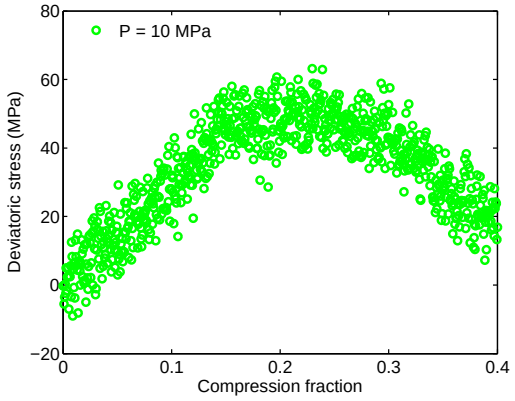

(c)

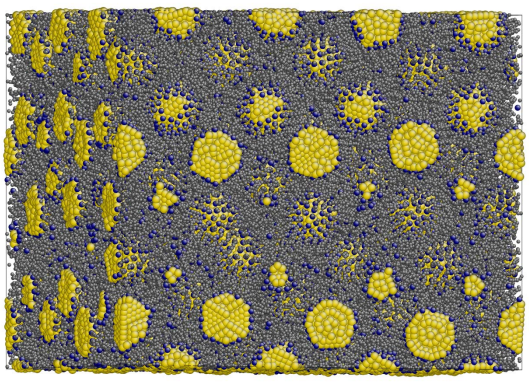

(d)

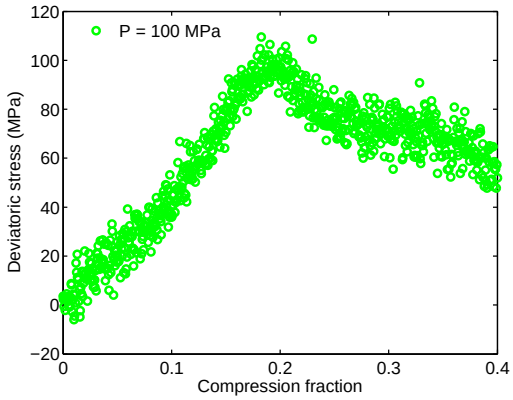

(e)

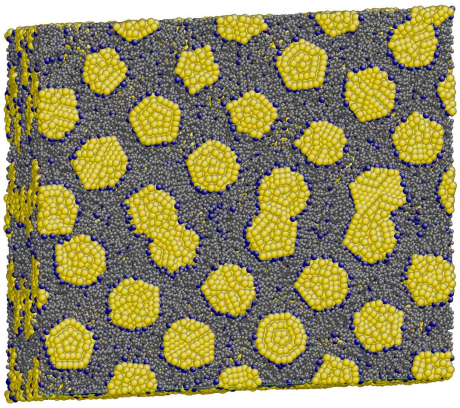

(f)

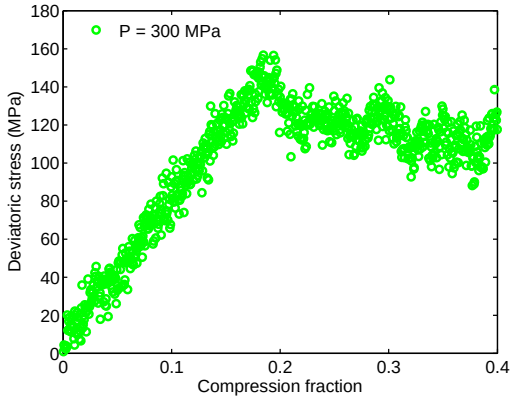

(g)

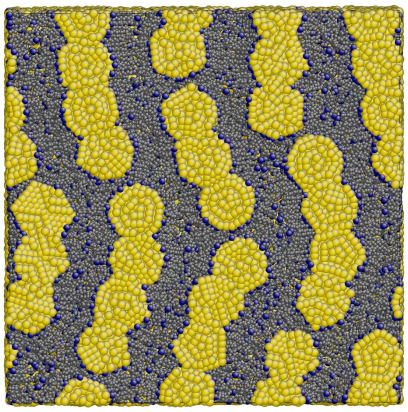

(h)

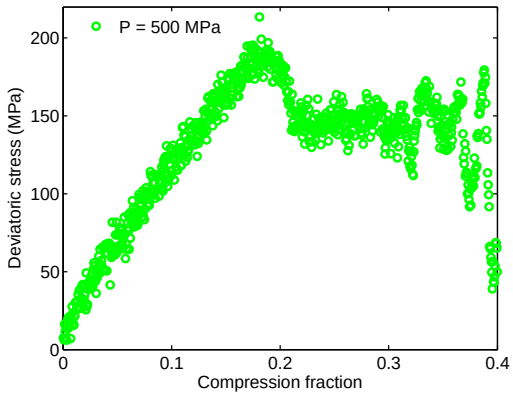

(i)

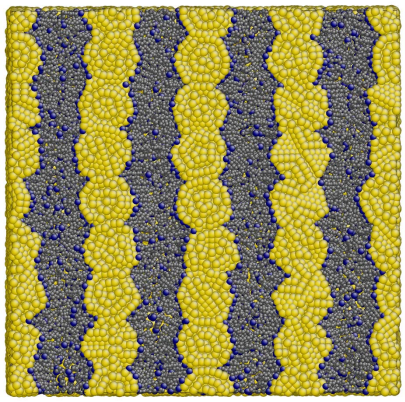

(j)

FIG. S2. **Deviatoric stress versus engineering strain curves and molecular configurations of the system at compression fraction equal to 0.4.** The left panels are stress-strain curves. The right panels are the corresponding configurations of the system. Simulation results are shown for (a-b): $P = 1$ MPa; (c-d): $P = 10$ MPa; (e-f): $P = 100$ MPa; (g-h): $P = 300$ MPa and (i-j): $P = 500$ MPa.

IV. COMPUTING THE ELASTIC CONSTANTS OF NANOPARTICLE SUPERLATTICES

We use strain-fluctuation method [28, 29] to compute the elastic constants of NPSL. Direct calculation of elastic constants from stress-strain curve for NPSL is challenging at finite temperature, due to the presence of thermal fluctuation which necessitates careful statistical averaging. The benefit of strain-fluctuation method is that full elastic tensor can be obtained in one simulation. However, strain-fluctuation method is known to converge very slowly. In our simulation, convergence of elastic constants computed via strain fluctuation method typically takes more than 10 nanoseconds after the simulation cell is fully equilibrated. We have confirmed that the elastic constants calculated using strain-fluctuation method is the same as those obtained via direct deformation in constant particle, constant volume and constant temperature (NVT) ensemble.

A. Elastic Constants in Voigt Notation

Before describing our calculation methodologies and simulation procedures, we present here some background information on the representation of elastic constants.

In linear elasticity, stress and strain are related by Hooke's law

$$\sigma_{ij} = \sum_{k,l} C_{ijkl}\epsilon_{kl}, \tag{10}$$

where σ_{ij} and ϵ_{kl} denote stress and strain tensor respectively. C_{ijkl} is the fourth-rank elastic stiffness tensor. Symmetry relations between the tensor elements allow the use of Voigt notation[1] to simplify Hooke's law. The indices mapping scheme in Voigt notation is shown in Table II:

TABLE II. Indices mapping in Voigt notation

Regular Index	11	22	33	23 or 32	13 or 31	12 or 21
Voigt Index	1	2	3	4	5	6

It then follows $C_{1111} = C_{11}$, $C_{1122} = C_{12}$, $C_{1123} = C_{14}$, $C_{2323} = C_{44}$, *etc.* The elements of stress tensor can be written in Voigt notation as $\sigma_{11} = \sigma_1$, $\sigma_{22} = \sigma_2$, $\sigma_{33} = \sigma_3$, $\sigma_{23} = \sigma_{32} = \sigma_4$,

[1] Lecture Notes by Professor Michael Demkowicz is gratefully acknowledged here

$\sigma_{13} = \sigma_{31} = \sigma_5$, $\sigma_{12} = \sigma_{21} = \sigma_6$. Elements of strain tensor can be written as $\epsilon_{11} = \epsilon_1$, $\epsilon_{22} = \epsilon_2$, $\epsilon_{33} = \epsilon_3$, $2\epsilon_{23} = 2\epsilon_{32} = \epsilon_4$, $2\epsilon_{13} = 2\epsilon_{31} = \epsilon_5$, $2\epsilon_{12} = 2\epsilon_{21} = \epsilon_6$. With this index transformation, Hooke's law becomes

$$\sigma_i = C_{ij}\epsilon_j, \tag{11}$$

where C_{ij} is now a 6×6 matrix. C_{ij}, the elastic constant matrix, is what we aim to compute from simulation.

We can invert Hooke's law as

$$\epsilon_i = S_{ij}\sigma_j. \tag{12}$$

S_{ij}, the compliance matrix, is the matrix inverse of C_{ij}. In Voigt notation, S_{ij} is related to S_{ijkl} (full compliance tensor) as:

$S_{mn} = 2S_{ijkl}$ if one and only one of m or n is equal to 4, 5, or 6;

$S_{mn} = 4S_{ijkl}$ if both m and n are equal to 4, 5, or 6;

$S_{mn} = S_{ijkl}$ otherwise.

The full compliance tensor S_{ijkl} is what we can obtain from strain-fluctuation method, which we will describe below. Once S_{ijkl} is known, the compliance matrix can be constructed via the above rules. The elastic constant matrix is then obtained by matrix inversion of S_{ij}.

B. Fluctuation and Elastic Constants in Molecular Dynamics Simulation

The fundamental equation employed in strain-fluctuation method is [28, 29]

$$\langle \epsilon_{ij}\epsilon_{kl} \rangle - \langle \epsilon_{ij} \rangle \langle \epsilon_{kl} \rangle = \frac{k_B T}{V} S_{ijkl}, \tag{13}$$

where k_B is the Boltzmann constant, V is the volume of the system; $\langle\,\rangle$ denotes ensemble average in constant temperature, constant stress (thermodynamic tension), and constant particle number (TtN) ensemble [30]. In practical molecular dynamics simulation, the size and shape of simulation box are allowed to change according to the method of Parrinello and Rahman [23, 24]. Let $h = \{\mathbf{a}, \mathbf{b}, \mathbf{c}\}$ represents matrix constructed from the supercell vectors $\mathbf{a}, \mathbf{b}$ and $\mathbf{c}$. The instantaneous strain tensor $\boldsymbol{\epsilon}$ is related to the h matrix as [29]

$$\boldsymbol{\epsilon} = \frac{1}{2}\left[(h_0^{-1})^{\mathrm{T}} h^{\mathrm{T}} h (h_0^{-1}) - I\right], \tag{14}$$

where h_0 is a reference matrix. In our case, h_0 is taken to be the time average of h. The superscript -1 and T stand for matrix inversion and transposition, respectively. I denotes

identity matrix. Running sufficiently long simulation after equilibration, one can compute $\langle \epsilon_{ij}\epsilon_{kl}\rangle$, $\langle \epsilon_{ij}\rangle\langle \epsilon_{kl}\rangle$ and average volume V. The compliance tensor S_{ijkl} is then calculated by Eq. 13. The elastic constant matrix C_{ij} can be obtained following the procedures described in the previous section.

The bulk modulus K can be calculated from volume fluctuations in molecular dynamics simulation. The fluctuation formula for bulk modulus is [31]

$$K = \frac{\langle V\rangle k_B T}{\langle V^2\rangle - \langle V\rangle^2} \tag{15}$$

C. Simulation Procedures for Calculation of Elastic Constants at Various Pressure

A gold NPSL system consisting of 2×2×2 *fcc* supercell was created by placing 32 gold nanoparticles $Au_{561}(SC_8)_{136}$ at the initial lattice positions, totaling 57120 (united) atoms. The configurations of individual gold nanoparticles were fully equilibrated at 300 K. In total, the superlattice contains 57120 (united) atoms. The relaxation procedures for superlattice are the same as described in the Simulation Methods section. Enlarging the system from a 2×2×2 supercell to a 3×3×3 supercell does not change the calculated elastic constants beyond convergence error limit.

For calculation of elastic constants under different hydrostatic pressure, we first raised the pressure of the system in the $T\mathbf{t}N$ ensemble to a target pressure P over a simulation period of 1 ns. The system was then equilibrated at P for 2 ns. Both the size and shape of the simulation box were allowed to change. σ_{xx}, σ_{yy} and σ_{zz} of the $T\mathbf{t}N$ ensemble were independently controlled at the target pressure, while σ_{xy}, σ_{yz} and σ_{xz} were independently controlled at zero. The simulation system was then fully equilibrated until potential energy and total volume of the system reach equilibrium values. This step took less than 1 ns when P is around ambient pressure but could take more than 10 ns when P is larger than 100 MPa, as we found higher pressure leads to slower relaxation dynamics of the ligands. Production run for computation of elastic constants took 15 ns to 20 ns for the elastic constants to converge. Fig. S3 shows the convergence plot of $\langle C_{11}\rangle$, $\langle C_{12}\rangle$, $\langle C_{44}\rangle$, and bulk modulus K at pressure $P = 100$ MPa. For cubic crystal, $C_{11} = C_{22} = C_{33}$, $C_{12} = C_{13} = C_{23}$, $C_{44} = C_{55} = C_{66}$. $\langle C_{11}\rangle$, $\langle C_{12}\rangle$ and $\langle C_{44}\rangle$ are defined as

$$\langle C_{11}\rangle = \frac{C_{11}+C_{22}+C_{33}}{3}, \quad \langle C_{12}\rangle = \frac{C_{12}+C_{13}+C_{23}}{3}, \quad \langle C_{44}\rangle = \frac{C_{44}+C_{55}+C_{66}}{3}. \tag{16}$$

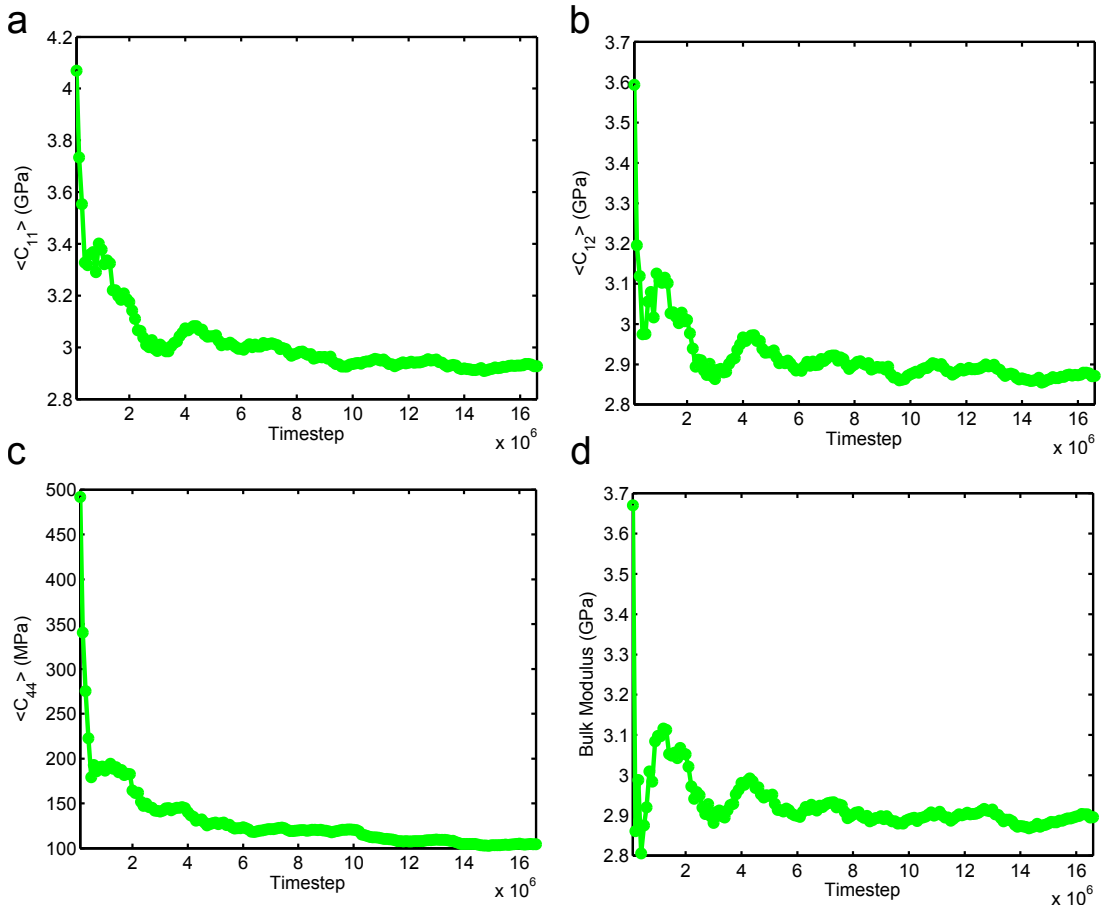

FIG. S3. **Convergence of elastic constants as a function of simulation timestep at $P =$ 100 MPa.** (a) $\langle C_{11} \rangle$, (b) $\langle C_{12} \rangle$, (c) $\langle C_{44} \rangle$ and (d) bulk modulus B.

---

[1] Plimpton, S. Fast parallel algorithms for short-range molecular dynamics. *J. Comput. Phys.* **117**, 1–19 (1995). See also `http://lammps.sandia.gov`.

[2] Lincoln, R. C., Koliwad, K. M. & Ghate, P. B. Morse-potential evaluation of second-and third-order elastic constants of some cubic metals. *Phys. Rev.* **157**, 463–466 (1967).

[3] Girifalco, L. A. & Weizer, V. G. Application of the Morse potential function to cubic metals. *Phys. Rev.* **114**, 687–690 (1959).

[4] Foiles, S. M., Baskes, M. I. & Daw, M. S. Embedded-atom-method functions for the fcc metals Cu, Ag, Au, Ni, Pd, Pt, and their alloys. *Phys. Rev. B* **33**, 7983–7991 (1986).

[5] Paul, W., Yoon, D. Y. & Smith, G. D. An optimized united atom model for simulations of polymethylene melts. *J. Chem. Phys.* **103**, 1702–1709 (1995).

[6] Kaushik, A. P. & Clancy, P. Explicit all-atom modeling of realistically sized ligand-capped nanocrystals. *J. Chem. Phys.* **136**, 114702 (2012).

[7] Allinger, N. L., Yuh, Y. H. & Lii, J. H. Molecular mechanics. The MM3 force field for hydrocarbons. 1. *J. Am. Chem. Soc.* **111**, 8551–8566 (1989).

[8] Häkkinen, H. The gold-sulfur interface at the nanoscale. *Nat. Chem.* **4**, 443–455 (2012).

[9] Zhang, L. Z., Goddard, W. A. & Jiang, S. Y. Molecular simulation study of the c(4×2) superlattice structure of alkanethiol self-assembled monolayers on Au(111). *J. Chem. Phys.* **117**, 7342–7349 (2002).

[10] Luedtke, W. & Landman, U. Structure, dynamics, and thermodynamics of passivated gold nanocrystallites and their assemblies. *J. Phys. Chem.* **100**, 13323–13329 (1996).

[11] Luedtke, W. D. & Landman, U. Structure and thermodynamics of self-assembled monolayers on gold nanocrystallites. *J. Phys. Chem. B* **102**, 6566–6572 (1998).

[12] Ghorai, P. K. & Glotzer, S. C. Molecular dynamics simulation study of self-assembled monolayers of alkanethiol surfactants on spherical gold nanoparticles. *J. Phys. Chem. C* **111**, 15857–15862 (2007).

[13] Schapotschnikow, P., Pool, R. & Vlugt, T. J. H. Molecular simulations of interacting nanocrystals. *Nano Lett.* **8**, 2930–2934 (2008).

[14] Beardmore, K. M., Kress, J. D., Gronbech-Jensen, N. & Bishop, A. R. Determination of the headgroup-gold (111) potential surface for alkanethiol self-assembled monolayers by *ab initio* calculation. *Chem. Phys. Lett.* **286**, 40–45 (1998).

[15] Liu, C. L., Cohen, J. M., Adams, J. B. & Voter, A. F. EAM study of surface self-diffusion of single adatoms of fcc metals Ni, Cu, Al, Ag, Au, Pd, and Pt. *Surf. Sci.* **253**, 334–344 (1991).

[16] Sheehan, P. E. & Whitman, L. J. Thiol diffusion and the role of humidity in "Dip Pen Nanolithography". *Phys. Rev. Lett.* **88**, 156104 (2002).

[17] Sellers, H., Ulman, A., Shnidman, Y. & Eilers, J. E. Structure and binding of alkanethiolates on gold and silver surfaces: implications for self-assembled monolayers. *J. Am. Chem. Soc.* **115**, 9389–9401 (1993).

[18] Zhang, W. *et al.* Electronic structure of [121] tetramantane-6-thiol on gold and silver surfaces. *J. Chem. Phys.* **130**, 054705 (2009).

[19] Hautman, J. & Klein, M. L. Simulation of a monolayer of alkyl thiol chains. *J. Chem. Phys.* **91**, 4994 (1989).

[20] Jorgensen, W. L., Madura, J. D. & Swenson, C. J. Optimized intermolecular potential functions for liquid hydrocarbons. *J. Am. Chem. Soc.* **106**, 6638–6646 (1984).

[21] Jorgensen, W. L., Maxwell, D. S. & Tirado-Rives, J. Development and testing of the OPLS all-atom force field on conformational energetics and properties of organic liquids. *J. Am. Chem. Soc.* **118**, 11225–11236 (1996).

[22] Landman, U. & Luedtke, W. D. Small is different: energetic, structural, thermal, and mechanical properties of passivated nanocluster assemblies. *Faraday Discuss.* **125**, 1–22 (2004).

[23] Parrinello, M. & Rahman, A. Crystal structure and pair potentials: A molecular-dynamics study. *Phys. Rev. Lett.* **45**, 1196–1199 (1980).

[24] Parrinello, M. & Rahman, A. Polymorphic transitions in single crystals: A new molecular dynamics method. *J. Appl. Phys.* **52**, 7182–7190 (1981).

[25] Martyna, G. J., Tobias, D. J. & Klein, M. L. Constant pressure molecular dynamics algorithms. *J. Chem. Phys.* **101**, 4177–4189 (1994).

[26] Shinoda, W., Shiga, M. & Mikami, M. Rapid estimation of elastic constants by molecular dynamics simulation under constant stress. *Phys. Rev. B* **69**, 134103 (2004).

[27] Tuckerman, M. E., Alejandre, J., López-Rendón, R., Jochim, A. L. & Martyna, G. J. A Liouville-operator derived measure-preserving integrator for molecular dynamics simulations in the isothermal–isobaric ensemble. *J. Phys. A-Math. Gen.* **39**, 5629–5651 (2006).

[28] Ray, J. R. Elastic constants and statistical ensembles in molecular dynamics. *Comput. Phys. Rep.* **8**, 111–151 (1988).

[29] Parrinello, M. & Rahman, A. Strain fluctuations and elastic constants. *J. Chem. Phys.* **76**, 2662–2666 (1982).

[30] Ray, J. R. & Rahman, A. Statistical ensembles and molecular dynamics studies of anisotropic solids. II. *J. Chem. Phys.* **82**, 4243–4247 (1985).

[31] Allen, M. P. & Tildesley, D. J. *Computer Simulation of Liquids* (Oxford Unviersity Press, 1989).